Journal of Advanced Ceramics
2021, **10**(2): 258–270
https://doi.org/10.1007/s40145-020-0436-z
ISSN 2226-4108
CN 10-1154/TQ

Research Article

Enhanced aging and thermal shock performance of $Mn_{1.95-x}Co_{0.21}Ni_{0.84}Sr_xO_4$ NTC ceramics

Haibing LI[a,b,c], Huimin ZHANG[a,*], Slapley THAYIL[c], Aimin CHANG[a,*], Xu SANG[a,b], Xiuhua MA[a,b]

[a]*Key Laboratory of Functional Materials and Devices for Special Environments of Chinese Academy of Sciences, Xinjiang Key Laboratory of Electronic Information Materials and Devices, Xinjiang Technical Institute of Physics & Chemistry of Chinese Academy of Sciences, Urumqi 830011, China*
[b]*University of the Chinese Academy of Sciences, Beijing 100049, China*
[c]*Xinjiang Research Institute of Measurement & Testing, Urumqi 830011, China*

Received: April 15, 2020; Revised: October 13, 2020; Accepted: November 9, 2020

Abstract: The $Mn_{1.95-x}Co_{0.21}Ni_{0.84}Sr_xO_4$ (MCNS) ($0 \leqslant x \leqslant 0.15$) based negative temperature coefficient (NTC) materials are prepared by co-precipitation method. The replacement of Mn by Sr plays a critical role in controlling the lattice parameter, relative density, microstructure, and electrical properties. The lattice parameter and relative density increase with the increase of Sr content. A small amount of Sr restrains the grain growth and increases the bulk density. Moreover, the room resistivity ρ_{25}, material constant $B_{25/50}$, activation energy E_a, and temperature coefficient α values of MCNS ceramics are influenced by the Sr content and ranged in 1535.0–2053.6 Ω·cm, 3654–3709 K, 0.3149–0.3197 eV, and (–4.173%)–(–4.111%), respectively. The X-ray photoelectron spectroscopy (XPS) results explain the transformation of MCNS ceramics from n- to p-type semiconductors. The conduction could arise from the hopping polaron between Mn^{3+}/Mn^{4+} and Co^{2+}/Co^{3+} in the octahedral sites. The impedance data analysis also discusses the conduction mechanism of the MCNS ceramic, whereas grain resistance dominates the whole resistance of the samples. Furthermore, the aging coefficient ($\Delta R/R$) of MCNS ceramics is found to be < 0.2%, which indicates the stable distribution of cations in the spinel. Finally, the MCNS ceramics demonstrate excellent thermal durability with < 1.3% of resistance shift after100 thermal shock cycles.

Keywords: Sr-doped Mn–Co–Ni–O materials; negative temperature coefficient (NTC) ceramics; electrical properties; thermal shock cycling

1 Introduction

Negative temperature coefficient (NTC) ceramic thermistors based on mixed-valence transition manganites are being widely employed in temperature sensors, controllers, infrared detectors, time delay, and voltage regulators [1–8].

The electrical properties of spinel Mn_3O_4, doped with different transition metal (Co, Ni, Zn, Fe, Cu) cations, are mainly influenced by the Mn^{3+}/Mn^{4+} couple at B-sites

* Corresponding authors.
E-mail: H. Zhang, zhanghm@ms.xjb.ac.cn;
A. Chang, changam@ms.xjb.ac.cn

and changed with dopant content [2,4–6,8]. Moreover, a ternary spinel compound, i.e., $(Mn_{3-x-y}Co_xNi_y)O_4$ (MCN), renders promising electrical properties due to easy fabrication and outstanding thermistor properties [9]. The electrical mechanism of MCN can be explained by small polaron hopping conduction [10]. Furthermore, the electrical properties of MCN can be tuned by doping small-sized transition metals at B-sites, such as Fe, Zn, and Cu [2,8,11,12]. Hence, the substituent Sr, which is a divalent ion with a larger radius than Mn, facilitates the conversion of Mn^{3+} to Mn^{4+}. Therefore, Sr-doping efficiently modifies the electrical properties of ceramic thermistors by inhibiting the migration of cationic vacancies and improving aging performance. Mohapatra *et al*. [13] have synthesized Sr-substituted polycrystalline $LiFe_5O_8$ spinel by solid-state method, resulting in improved dielectric and magnetic properties. Furthermore, Zhao *et al*. [14] have prepared $La_{0.7}(Ca_{0.3-x}Sr_x)MnO_3$ ($0 \leqslant x \leqslant 0.3$) using the sol–gel method and improved the electrical and magnetic properties due to Sr-induced double-exchange interactions. Wang *et al*. [15] have fabricated Sr-doped $Bi_4Ti_3O_{12}$ ceramics by solid-state reaction method and suppressed the dielectric dispersion due to Sr-induced defect compensation. Nevertheless, the NTC behavior of MCNS ceramics has rarely been reported [16].

Moreover, the industrial applicability of advanced ceramics requires long-time thermal durability under different conditions, such as constant and variable temperatures. Recently, Yang and Liu [17] have investigated the microstructural evolution and mechanical behavior of oxide/oxide ceramic matrix composites under cyclic thermal shocks, demonstrating an increase in microcrack density under thermal shock. Parvanian *et al*. [18] have characterized the pore structure of open-cell silicon carbide (SiC)-based foams and evaluated the mechanical performance before and after thermal shock testing. Liao *et al*. [19] have synthesized multi-walled carbon nanotubes (MWCNTs)-enhanced Si_2BC_3N ceramics by spark plasma sintering (SPS) and demonstrated improved thermal stress resistance due to the presence of MWCNTs. It can be concluded that the formation of microcracks or pores under thermal shock greatly influences the electrical properties of NTC ceramic thermistors. However, the influence of cyclic thermal shocks on the thermal stability of NTC ceramics has not been studied yet. Herein, Sr-substituted MCN ceramics are synthesized by the co-precipitation method, and the structure, microstructure, and electrical properties are systematically explored. Besides, the thermal shock testing is used to characterize the thermal stability of ceramic materials.

2 Experimental

The Sr-doped MCN oxide, with chemical composition of $Mn_{1.95-x}Co_{0.21}Ni_{0.84}Sr_xO_4$ (x = 0, 0.05, 0.1, and 0.15, labeled as A0, A1, A2, and A3 respectively), was obtained by co-precipitation method. Briefly, the comm.-ercially available nickel acetate, cobalt acetate, manganese acetate, and sodium hydrate were used as raw materials, whereas strontium acetate was used for Sr-doping. First, the stoichiometric mixture solution of nickel acetate, cobalt acetate, manganese acetate, and strontium acetate was prepared by using the deionized water. The sodium hydrate solution (2 M) was used, as a precipitation agent, into the solution mentioned above (1 M) at 50 ℃ under continuous stirring. The whole reaction was carried out for 10 h. Finally, the precipitate was filtered, washed, and dried at 80 ℃ for 12 h. The as-obtained precursor was ball-milled for 12 h and calcined in a muffle furnace at 800 ℃ for 4 h. The calcined powder was ground in an agate mortar for 12 h and pressed into pellets with a diameter of 10 mm and thickness of 2 mm. The pellets were sintered at 1175 ℃ for 2 h. Finally, the silver paste was coated on both surfaces of the sintered pellets and heated at 850 ℃ for 20 min.

The A0, A1, A2, and A3 powders were analyzed by thermogravimetric and differential thermal analysis (TG/DTA, NETZSCH STA 449C) in the temperature range of 30–1200 ℃ in air. The temperature was increased at the heating rate of 10 ℃/min. The crystalline structure was determined by X-ray diffraction (XRD, Bruker D8 Advance). The X-ray diffractometer is equipped with Cu Kα (λ = 1.5418 Å) radiation and a nickel filter. The XRD patterns were recorded in the angular range of 10°–80° (2θ). The microstructure of the samples was observed by using a scanning electron microscope (SEM, ZEISS SUPRA55VP), equipped with energy dispersive spectroscopy (EDS, Bruker Nano GmbH Berlin, Germany) for elemental analysis. The valence state of cations was investigated by X-ray photoelectron spectroscopy (XPS, Thermo Scientific Escalab 250xi), equipped with Al Kα radiation. The complex impedance spectrum was performed in the frequency range from 20 Hz to 120 MHz, using an impedance analyzer (E4990A, KEYSIGHT Technologies) controlled by a computer. The resistance was measured

in the temperature range of (–30)–70 ℃ by Agilent 34970A digital multimeter. The sample was immersed in absolute alcohol to minimize the temperature fluctuations (< ±0.05 ℃). The aging performance was assessed at 125 ℃ in a temperature-controlled furnace. Briefly, the sample was subjected to 100 thermal shock cycles and the low and high temperatures were fixed at –30 and 70 ℃, respectively. The dwelling time at each temperature was 10 min, whereas the dwelling time at ambient temperature was 15 min. The testing equipment and temperature-cycling profile are shown in Fig. 1.

3 Results and discussion

3.1 TG/DTA analysis

Figure 2 presents the TG and DTA curves of the A2 hydroxide precursor in the temperature range of room temperature (RT)–1200 ℃. The DTA curve exhibits an endothermic peak at 125 ℃, and an initial weight loss of 5.07% in the temperature range from RT to 200 ℃, which can be ascribed to the removal of water adsorbed by hydroxide and crystal lattice. In the temperature range of 200–800 ℃, A2 ceramic rendered a weight loss of 15.44% due to the decomposition of precursor and formation of the MCN phase. Moreover, the exothermic (EXO) peak in the DTA curve indicates the decomposition of the precursor. In the next step, the further increase in temperature (> 800 ℃) resulted in a weight loss of 1.82% due to the reduction of Mn^{4+} into Mn^{3+} [11,20]. Also, a broad endothermic peak at ~1100 ℃ can be attributed to the stable formation of MCNS ceramics due to cation redistribution.

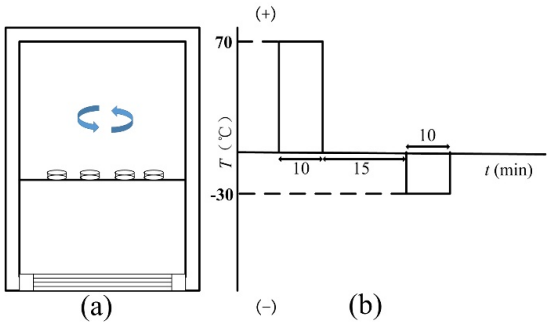

Fig. 1 Schematic illustration of (a) thermal shock equipment and (b) temperature-cycling profile.

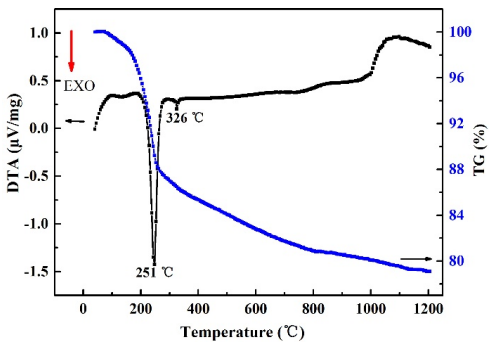

Fig. 2 TG/DTA curves of the A2 sample.

3.2 Structure and density analysis

The influence of calcination temperature on the phase composition of A2 precursor is shown in Fig. 3. Apparently, the calcination at 700 ℃ resulted in a mixture of cubic *Fd*3*m* spinel-type (JCPDS No. 01-1110) and hexagonal *P*63/*mmc* perovskite-type phases (JCPDS No. 72-0197). In the temperature range of 800–1175 ℃, the A2 precursor exhibited a single-phase cubic spinel structure, which is mainly characterized by distinct diffraction peaks at 2θ = 18.3° (111), 30.1° (220), 35.5° (311), 37.1° (222), 43.2° (400), 53.5° (422), 57.1° (511), 62.7° (440), and 74.1° (533). Note that the solubility of Sr improved with increasing calcination temperature, resulting in the formation of a single-phase cubic structure. Therefore, 800 ℃ is chosen as the calcination temperature.

The XRD patterns of single-phase MCNS ceramics, obtained with different amounts of Sr-doping, are shown in Fig. 4, confirming that the cubic structure is maintained after doping with Sr. Moreover, the typical diffraction peak of MCNS ceramics shifted towards lower diffraction angles with increasing concentration of Sr, which can be ascribed to the larger ionic radius Sr comparing to Mn or Co. Furthermore, the (311) peak of A3 ceramic shifted towards a higher diffraction angle, which is beyond the expectation. However, the observed phenomena are likely to be associated with the conversion of Co^{2+} to Co^{3+}, where the ionic radius

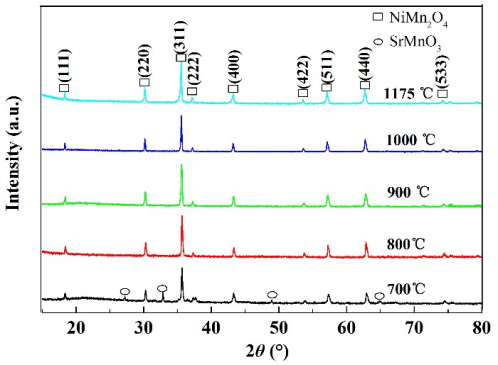

Fig. 3 XRD patterns of A2 ceramic at different temperatures.

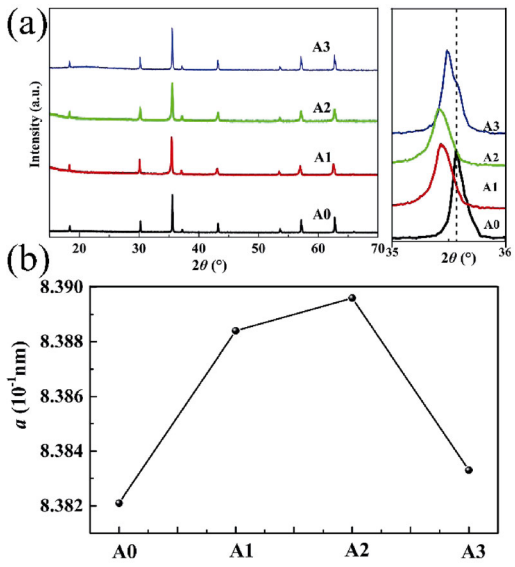

Fig. 4 (a) XRD patterns and (b) lattice parameters of A0, A1, A2, and A3 ceramics after sintering at 1175 ℃.

is decreased from 0.745 to 0.61 Å [21,22]. The lattice parameter (a) is fitted using a Powdercell software with Least Square Method [23,24], as shown in Fig. 4(b) and Table 1, which increased from 8.3821 to 8.3896 Å with increasing the Sr content from 0 to 0.1, respectively. On the other hand, the lattice parameter decreased to 8.3833 Å at x = 0.15, indicating the solubility limit of Sr (x = 0.1). The X-ray density (ρ_x) can be calculated from the given relationship:

$$\rho_x = \frac{Z \cdot M}{N \cdot V} \tag{1}$$

where Z refers to the number of molecules per unit cell (herein, Z = 8), M represents the molecular weight, N denotes the Avogadro constant, and V corresponds to the unit cell volume ($V = a^3$, cubic phase). The ρ_x of A0, A1, A2, and A3 ceramics increased from 5.251 to 5.276, 5.31, and 5.359 g/cm^3, respectively. The difference in ρ_x can be explained by the difference in atomic weight of different ions ($M_{Sr} > M_{Mn}$). The lattice parameter, crystal phase, and ρ_x of A0, A1, A2, and A3 ceramic samples are presented in Table 1.

Table 1 Lattice parameter, crystal phase, and ρ_x of A0, A1, A2, and A3 ceramic samples

Ceramic sample	Lattice parameter (Å)	Phase	ρ_x (g/cm^3)
A_0 (x = 0)	8.3821	Cubic spinel	5.251
A_1 (x = 0.05)	8.3884	Cubic spinel	5.276
A_2 (x = 0.1)	8.3896	Cubic spinel	5.310
A_3 (x = 0.15)	8.3833	Cubic spinel	5.359

The relative density (ρ_{rel}) can be given as

$$\rho_{rel} = \rho_b / \rho_x \tag{2}$$

where ρ_b refers to the bulk density, which is determined by the Archimedes method. The change in ρ_b with respect to Sr^{2+} content is illustrated in Fig. 5. Obviously, the ρ_b of A0–A3 ceramics linearly increased with increasing Sr concentration from 5.057 to 5.1774 g/cm^3, respectively. Figure 5 shows that the relative density of A0, A1, and A2 ceramics linearly increased from 96.3% to 96.8% with increasing Sr content from 0 to 0.1 respectively, and decreased to 96.4% at x = 0.15.

3. 3 Surface morphology analysis

Figures 6(a) and 6(b) show the SEM images of A2 ceramic after sintering at 1150 and 1175 ℃, respectively. Herein, the density and grain size increased with increasing sintering temperature. Secondary electron image (SEI) and elemental mapping were used to determine the distribution of different elements, as shown in Fig. 6(c). The element maps show that Mn, Co, Ni, Sr, and O are homogeneously distributed in A2 ceramic after sintering at 1175 ℃, which is selected as the sintering temperature in subsequent experiments.

Figure 7 presents surface morphologies of MCNS ceramics after sintering at 1175 ℃, showing high density and regular morphology. Nonetheless, it can be seen that the grain size of ceramics decreased from 10–12 μm (A0) to 3–4 μm (A2) after doping with Sr, indicating that a small amount of Sr dopant hinders the grain growth during sintering due to the dragging effect [25]. On the other hand, the surplus Sr in A3 ceramic may cluster at the grain boundaries and could improve the transport rate for grain coarsening [26]. Therefore, the A3 ceramic exhibited distinct grain boundaries with some undesirable pores. It is worth emphasizing that an optimal amount of dopant is required to achieve the desired densification and avoid grain coarsening [27,28].

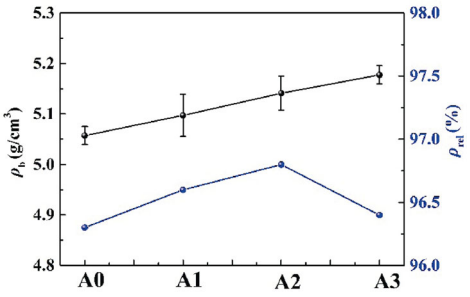

Fig. 5 ρ_b and ρ_{rel} of A0, A1, A2, and A3 NTC ceramics.

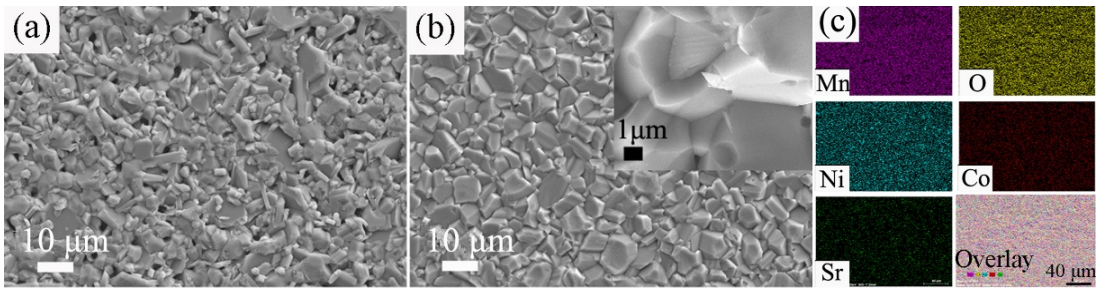

Fig. 6 SEM images of the A2 ceramic after sintering at (a) 1150 and (b) 1175 ℃ (the inset shows the corresponding cross-sectional SEM image). (c) EDS maps of different elements.

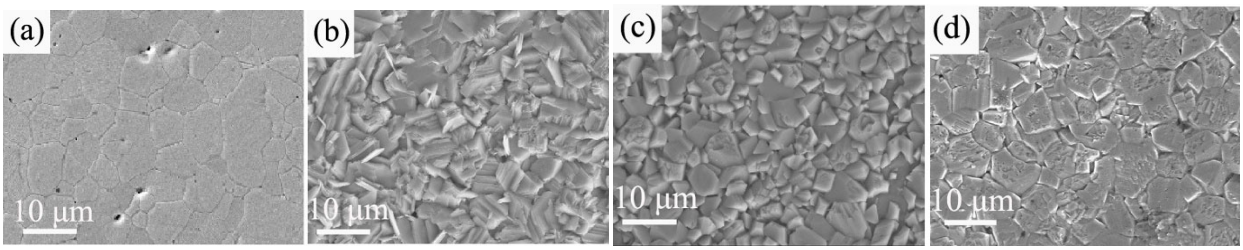

Fig. 7 Surface morphologies of (a) A0, (b) A1, (c) A2, and (d) A3 ceramics after sintering at 1175 ℃.

3. 4 Electrical characterization, XPS, and complex impedance analysis

The relationship between resistivity and absolute temperature of MCNS ceramics is shown in Fig. 8(a). The resistivity (ρ) of MCNS ceramics exponentially decreased with increasing temperature, which can be given by the Arrhenius equation:

$$\rho = \rho_0 \exp(B/T) = \rho_0 \exp(E_a/k_B T) \quad (3)$$

where ρ_0 represents the resistivity at an infinite temperature ($T \to \infty$), T corresponds to the absolute temperature, and B denotes the material constant, as given by Eq. (3), E_a refers to the activation energy, and k_B represents the Boltzmann constant. The $B_{25/50}$ constant can be given as

$$B_{25/50} = \frac{\ln(R_{25}/R_{50})}{1/T_{25} - 1/T_{50}} \quad (4)$$

where R_{25} and R_{50} represent the resistance of ceramic at 25 and 50 ℃, respectively. Figure 8(b) shows the relationship between lnρ and reciprocal of absolute temperature (1000/T) of MCNS ceramics. The room-temperature resistivity, thermal constant, activation energy, and temperature coefficient of MCNS ceramics are summarized in Table 2.

As shown in Table 2, the ρ_{25}, $B_{25/50}$, E_a, and α values of as-prepared MCNS ceramics are in the range of 1535.0–2053.6 Ω·cm, 3654–3709 K, 0.3149–0.3197 eV, and (–4.173%)–(–4.111%), respectively, after sintering

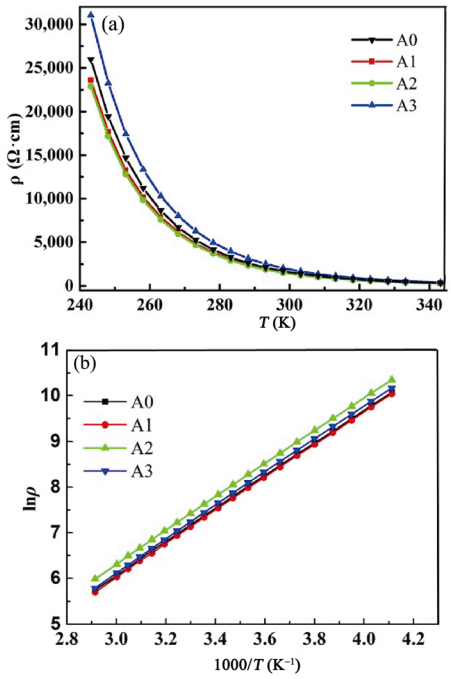

Fig. 8 Relationship between (a) resistivity (ρ) and absolute temperature (T), and (b) lnρ and reciprocal of absolute temperature (1000/T) of A0, A1, A2, and A3 ceramics.

Table 2 Room-temperature resistivity (ρ_{25}), B constant, E_a, and temperature coefficient (α) of MCNS ceramics

Ceramic sample	ρ_{25} (Ω·cm)	$B_{25/50}$ (K)	E_a (eV)	α (%)
A0	1707.9	3676	0.3168	–4.136
A1	1590.3	3667	0.3160	–4.111
A2	1535.0	3654	0.3149	–4.125
A3	2053.6	3709	0.3197	–4.173

at 1175 ℃. The resistivity initially decreased from 1707.9 to 1535.0 Ω·cm with increasing Sr content from 0 to 0.1, respectively, followed by an increase to 2053.6 Ω·cm at x = 0.15. The linear relationship between lnρ and 1000/T shows the characteristics of small-polaron hopping transport, which is often observed in Mn-based spinel structures (Fig. 8(b)). The MCNS spinel phase contains Mn element with different valence states, which facilitates electron jumping between Mn^{3+} and Mn^{4+} ions at octahedral sites [2,11]. As mentioned above, the NTC thermistor characteristics are described by the Nernst–Einstein relationship:

$$\sigma = \frac{N_{\text{oct}} e^2 d^2 \upsilon_0}{kT} NC(1-C)\exp\left(\frac{-E_{\text{a}}}{kT}\right) \quad (5)$$

where N_{oct} refers to the concentration of octahedral sites per cubic centimeter; e represents the unit charge; d represents the jumping distance for charge carriers; υ_0 denotes the lattice vibrational frequency (which is associated with conduction); e represents the electronic charge; N denotes the concentration of per formula unit of sites, which are available for the charge carriers; C is the ratio of available sites occupied by the charge carriers, $NC(1–C)$ is related to the number of Mn^{3+} and Mn^{4+} cations at octahedral sites.

In the next step, XPS analysis was carried out to quantify the Mn^{3+}/Mn^{4+} and Co^{3+}/Co^{2+}couple and to clarify the mechanism of resistivity variation.

The chemical components and elemental valence of the A0, A1, A2, and A3 samples are characterized by XPS spectra (Figs. 9 and 10). In the XPS spectra of sample A0 from Fig. 9(a), the Ni $2p_{3/2}$ peak and its satellite peak are located at the binding energies of 855.0 and 861.0 eV, respectively, and the Ni $2p_{1/2}$ peak and its satellite peak are located at the binding energies of 872.7 and 879.0 eV, respectively. These peaks are in agreement with the one reported by Pugaczowa-Michalska *et al*. [29], implying the only one kind of Ni ion such as Ni^{2+} exists in A0 ceramic. In the Sr^{2+}-doped ceramics, the Ni^{2+} ion can also be detected, although the related peaks have about 0.3 eV shift towards lower binding energies compared with sample A0 [30]. The area of each peaks have changed little, indicating the constant Ni ion content. From Fig. 9(b) of Co 2p spectra, the $2p_{3/2}$ and $2p_{1/2}$ peaks are fitted by two peaks, which are according to Co in octahedral (B) and tetrahedral (A) sites. The peaks at 780.1 and 795.7 eV are corresponding to the Co in octahedral sites, the peaks at 782.4 and 798.3 eV are assigned to the Co in tetrahedral sites, while the peaks at 786.4 and 802.6 eV are their satellite peaks [31,32]. The respective satellite peaks of $2p_{3/2}$ and $2p_{1/2}$ are fitted using one peak each. The ratios of the respective area under the curves are tabulated in Table 3, and the ratio of Co^{3+} and Co^{2+} in the ceramic samples can be obtained by using of the area of the satellite peaks. Finally, the ratio of Co in A site and B site (Co_A/Co_B) for A0, A1, A2, and A3 ceramics was calculated to be 0.37, 0.41, 0.34, and 0.27, respectively. Hence, the Co^{3+}/Co^{2+} ratio in A0, A1, A2, and A3 ceramics was found to be 0.15, 0.14, 0.12, and 0.11, respectively. It suggested that the redistribution of Co in the octahedral and tetrahedral sites occurs, as well as conversion of equivalent amount of Co^{2+} to Co^{3+}, indicating that more Co^{2+} are converted to Co^{3+}. The experimental data were normalized by the least square procedure and peak intensities of Mn^{2+} (641.2 eV), Mn^{3+} (642.4 eV), and Mn^{4+} (643.8 eV) were calculated [33,34], as shown in Fig. 10. It can be concluded that the ratio of Mn^{2+}, Mn^{3+}, and Mn^{4+} ions in different ceramics is equal to the ratio of peak areas, respectively. Hence, the Mn^{3+}/Mn^{4+} ratio in A0, A1, A2, and A3 ceramics was found to be 1.24, 1.66, 1.67, and 1.40, respectively (Table 3). The Co^{3+}/Co^{2+} ratio gradually decreased with increasing Sr, while the Mn^{3+}/Mn^{4+} ratio initially increased with increasing Sr content, followed by a decrease at x = 0.15.

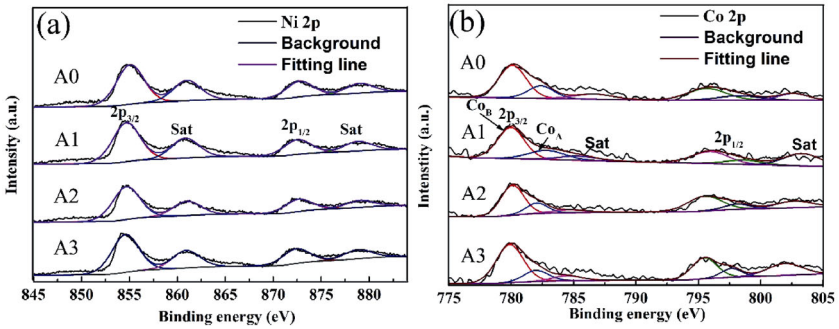

Fig. 9 XPS spectra of (a) Ni 2p and (b) Co 2p from A0, A1, A2, and A3 ceramics.

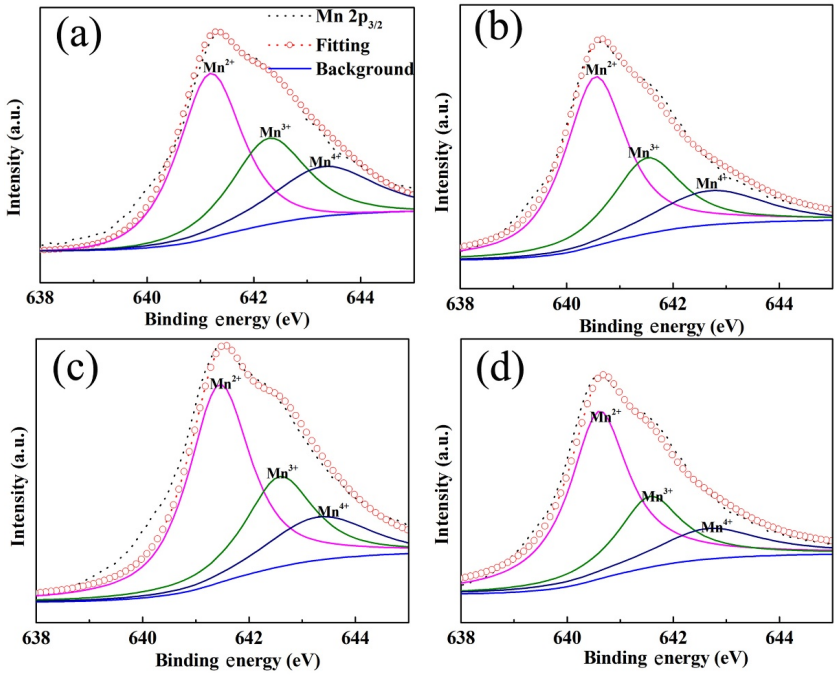

Fig. 10 High-resolution Mn $2p_{3/2}$ XPS spectra from (a) A0, (b) A1, (c) A2, and (d) A3 ceramics.

Table 3 Relative concentration of Co, Mn ions, and thermopower *Q* values in different ceramics

Ceramic sample	Co 2p		Mn 2p				*Q* (μV)
	Co_A/Co_B	Co^{3+}/Co^{2+}	Mn^{2+} (%)	Mn^{3+} (%)	Mn^{4+} (%)	Mn^{3+}/Mn^{4+}	
A0	0.37	0.15	47.1	29.3	23.6	1.24	–0.69
A1	0.41	0.14	54.9	28.2	17.0	1.66	24.4
A2	0.34	0.12	54.8	28.2	16.9	1.67	25.0
A3	0.27	0.11	56.1	25.6	18.3	1.40	9.77

Sr^{2+} can occupy the octahedral or tetrahedral sites in MCNS as the interstitial occupancy is not allowed due to the large ionic size. To maintain the electrical neutrality, the incorporation of Sr leads to the following reaction [15,35]:

$$2SrO \rightarrow 2Sr'_{Mn} + 2O + V_O^{**} \quad (6)$$

Hence, Sr-doping facilitates the formation of oxygen vacancies. It has already been reported that more oxygen vacancies exist in grains of 0.05% Sr sample than MCN. Moreover, the re-oxidation reaction eliminates oxygen vacancies and produces holes in the grain boundaries during the cooling process, as given below [36,37]:

$$V_O^{**} + \frac{1}{2}O_2 \rightarrow O_O^{\times} + 2h^* \quad (7)$$

In order to keep the charge neutrality, the resulting holes could combine with Mn^{3+} ($Mn^{3+} + h^* \rightarrow Mn^{4+}$) or Co^{2+} ($Co^{2+} + h^* \rightarrow Co^{3+}$) and influences the resistivity according to the Nernst–Einstein relationship. Hence, Sr-doping lowered the resistivity of Sr-doped MCN ceramics for A1 sample, because the Mn^{3+} increased significantly but Co^{2+} changed negligibly. With increasing the content of Sr, migration of some Co ions from A sites to B sites has occurred. For A2 and A3 samples, the Co^{2+} in B site increased, combining with an increase Co^{2+}/Co^{3+} ions in octahedral, and it is well supported also by XRD analysis (decrease in the lattice parameter). To preserve the overall electrical neutrality, some Mn^{4+} converts to Mn^{3+}, and induces a decrease in the amount of Mn^{3+}/Mn^{4+}, which increases the resistivity of A3 ceramic [38]. These results are in good agreement with XPS analysis. Moreover, it can be seen that the electrons migrate through the shortest contact point between the particles. Therefore, the pores located at the grain boundaries increase the electron transportation distance between Mn^{3+} and Mn^{4+} ions according to Eq. (5). Consequently, the long transportation distance in hopping of carriers increases the resistivity and E_a, as shown by the A3 ceramic, which is an agreement with the results of the impedance spectroscopy of A3 sample, as shown in Fig. 11 [39].

For NTC ceramic, the "choice" between n- or p-type is largely depended on the small polaron carrier. Yokoyama *et al.* [40] synthesized the $Mn_{2-x}Co_{2x}Ni_{1-x}O_4$ spinel type oxide, and concluded that the oxides with $x = 0$ and $x = 0.25$ were n-type conductors. The

$Mn_{1.95}Co_{0.21}Ni_{0.84}O_4$ is similar with this composition, and the major carrier is also the electron. However, Sr^{2+} ions doped into the MCNS may act as the semiconducting acceptors and lead to the formation of conduction holes, followed by the p-type conductor. The transition process can be explained by Eqs. (6) and (7). It is worth noting that the carrier-type can also be calculated using the ratio of Mn^{3+}/Mn^{4+} ratio through the thermopower value Q, which can be defined as $Q=(k/e)\ln\left[\frac{1}{\beta}\frac{(Mn^{3+})}{(Mn^{4+})}\right]$, where $\beta=\frac{5}{4}$ denotes the spin degeneracy factor. The A0, A1, A2, and A3 ceramics rendered a Q of –0.69, 24.4, 25.0, and 9.77 μV, respectively, showing a transition from n- to p-type semiconducting behavior [10,41].

Impedance spectroscopy (IS) is a powerful tool for investigation of electrical behavior of ceramic samples, as a success of semicircle represents the grain effect, grain boundary effect, and electrode interfacial phenomena. The complex impedance spectra of A0, A1, A2, and A3 ceramic samples obtained at RT is shown in Fig. 11. With different Sr-doped contents, the spectrum displays depressed semicircle arches [42,43]. An equivalent circuit (the inset in Fig. 11(a)) modelled by ZSimDemo software was used to fit the IS data. Herein, R_g and R_{gb} represent the grain resistance and grain boundary resistance, and CPE is the constant phase element from grain boundary, which can be defined as $Z_{CPE}=1/(j\omega)^n$ [44], where j is the imaginary factor, $j=\sqrt{-1}$, and ω is the angular frequency ($\omega=2\pi f$, f is the frequency in Hz). The n represents the rotation angle according to the impedance response of ideal capacitor, and the value usually ranges between 0.5 and 1. For this reason, CPE is applied as flexible parameter to fit the impedance data. From Fig. 11, the simulated curve fitted the IS data well, reflecting that each impedance spectrum consists two parts reflecting the grain and grain boundary effect. Table 4 shows the fitted R_g, R_{gb}, and parameter n for A0, A1, A2, and A3 ceramics at RT. The R_g and R_{gb} both decrease from A0 to A2, then increase for A3 sample. It can be seen that the R_{gb} is higher than R_g for each sample at RT, suggesting the R_{gb} dominates the total of MCNS ceramics [45].

Moreover, based on Fig. S1 in the Electronic Supplementary Material, Fig. 12 shows the temperature dependence of the R_g and R_{gb} obtained by the equivalent circuit fitting for the MCNS ceramic. All of $\ln R_{gb}$ and $\ln R_g$ present obvious NTC characteristics. Besides, the E_a of grain and grain boundary for ceramic sample can be obtained, and their values are 0.3064 and 0.3359 eV, suggesting that the grain boundary needs higher E_a for hopping than the grain [46]. The conductance of the grains and grain boundaries is caused by hole carrying hopping. It could be explained by the activation energy, because the activation energy of the grains and grain boundaries is lower than the activation energy of oxygen vacancies [47,48]. Combining with the IS analysis, the conductive mechanism for NTC ceramic would improve the application for industry thermistors.

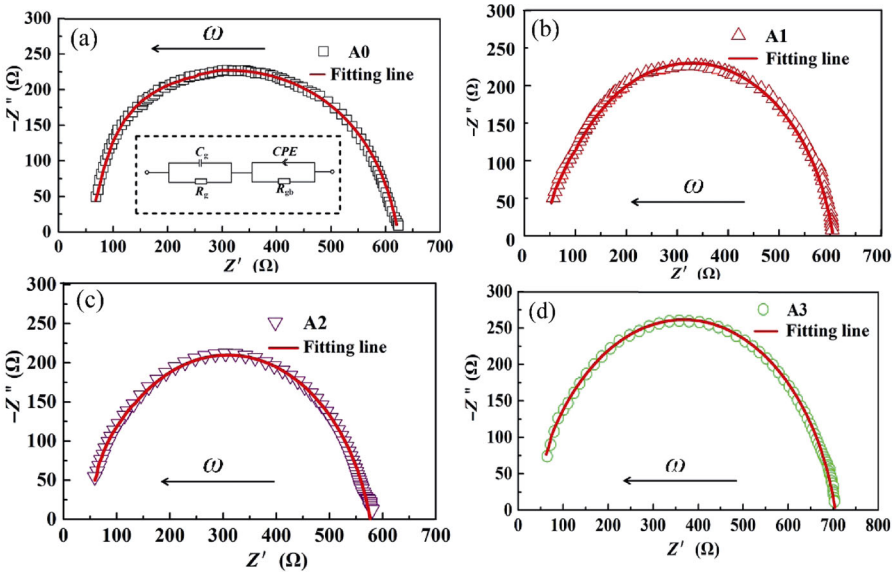

Fig. 11 Impedance spectroscopies of MCNS ceramics: (a) A0 (with the equivalent circuit for fitting the impedance data in the inset), (b) A1, (c) A2, and (d) A3 ceramics at RT.

Table 4 Fitted R_g, R_{gb}, and parameter n for A0, A1, A2, and A3 ceramics at RT

Sample	A0	A1	A2	A3
R_g (Ω)	57.2	49.0	43.9	51.3
R_{gb} (Ω)	579.3	529.0	535.3	681.1
n	0.81	0.89	0.86	0.81

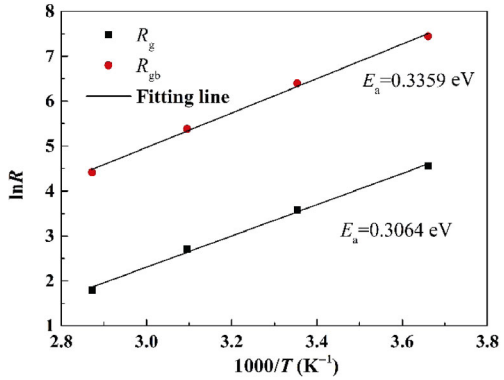

Fig. 12 Temperature dependence of impedances from R_g and R_{gb} for A2 sample.

3. 5 Aging performance and thermal shock cycling

Furthermore, the aging performance of MCNS ceramics at 125 ℃, has been assessed by resistance variation and the results are shown in Fig. 13. We have observed that the variation of aging coefficient ($\Delta R/R$) ranged from 0.16% to 1.31% during 1000 h. However, the relative resistance drift is found to be smaller in Sr-doped MCNS at x = 0.1. Figure 14 shows the relative resistance variation of MCNS ceramics with different numbers of thermal shock cycles. The relative resistance shifts were found to be 1.3%–8.9% after 100 thermal shock cycles. The resistance of MCNS ceramics significantly changed with the increasing number of thermal shock cycles but attained an almost constant value after 50 cycles. Hence, a small amount of Sr-doping can significantly improve the aging and cyclic thermal performance of MCNS ceramics. It is interesting that the single-phase Sr-doped MCN ceramics do not exhibit aging [49]. However, the large amount of dopant results in a deviation from the dense microstructure and compromises the aging performance. Moreover, the cationic vacancies diffuse into octahedral sites within the grains and increase the resistance. The addition of Sr decreases the concentration of cationic vacancies at the grain boundaries. Consequently, the inhibition of cationic vacancy diffusion significantly improves aging performance [50,51].

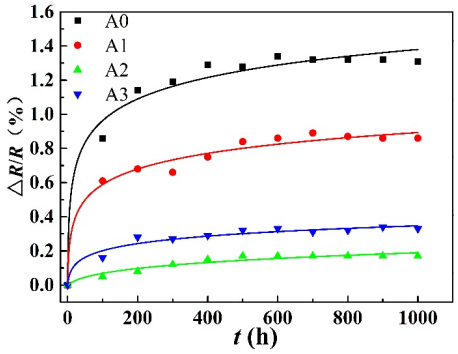

Fig. 13 Relative resistance drift of MCNS ceramics at 125 ℃ of 1000 h.

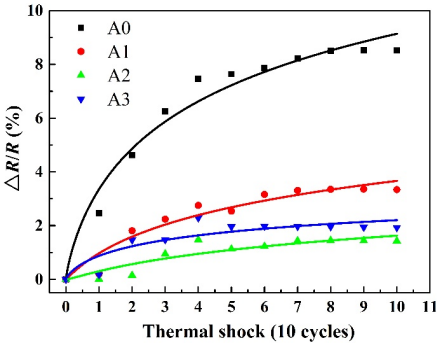

Fig. 14 Relative resistance drift of MCNS ceramics under thermal shock cycles.

XRD patterns of A0 ceramic have been recorded during aging after 0 h, 1000 h, and 100 thermal shock cycles. The results revealed that the A0 ceramic maintained the spinel structure after aging for 1000 h (Figs. 15(a) and 15(b)), whereas a rock salt phase appeared after 100 thermal shock cycles due to the segregation of NiO phase (Fig. 15(c)). In the case of A2 ceramic, the cubic spinel structure is maintained after aging for 1000 h and 100 thermal shock cycles. However, the diffraction peak at 2θ = 35.5°, corresponding to (311) planes of the spinal phase, has been shifted towards a higher diffraction angle after 100 thermal shock cycles, which is likely to be associated with the conversion of Co^{2+} to Co^{3+}.

The A2 ceramic surface does not exhibit any noticeable change after long time aging, as shown in Figs. 16(b) and 16(c). Meanwhile, the SEM images of the A2 ceramic were taken after 30 and 50 thermal shock cycles (Figs. 16(d) and 16(e)). However, the pores started to appear after 30 cycles and increased after 50 cycles, as shown in Figs. 16(d) and 16(e). Hence, the thermal shock testing resulted in pore formation and decreased the densification of A2 ceramic. The increment porosity caused by thermal

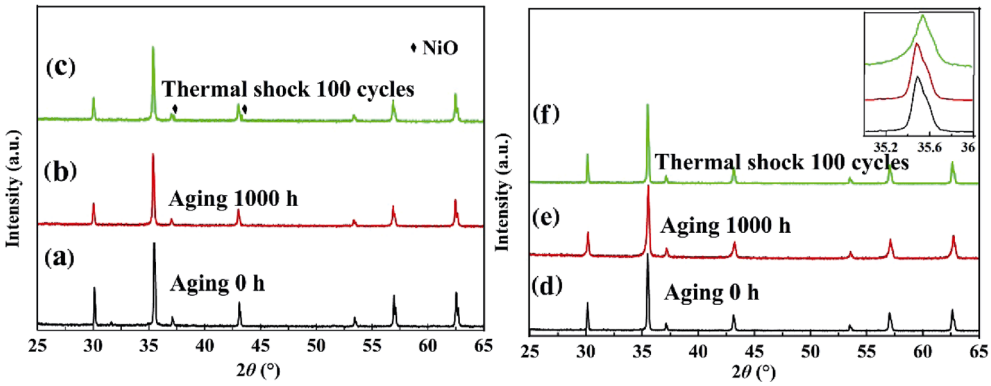

Fig. 15 XRD patterns of A0 ceramic after the aging process after (a) 0 h, (b) 1000 h, and (c) 100 thermal shock cycles, and A2 ceramic during aging after (d) 0 h, (e) 1000 h, and (f) 100 thermal shock cycles.

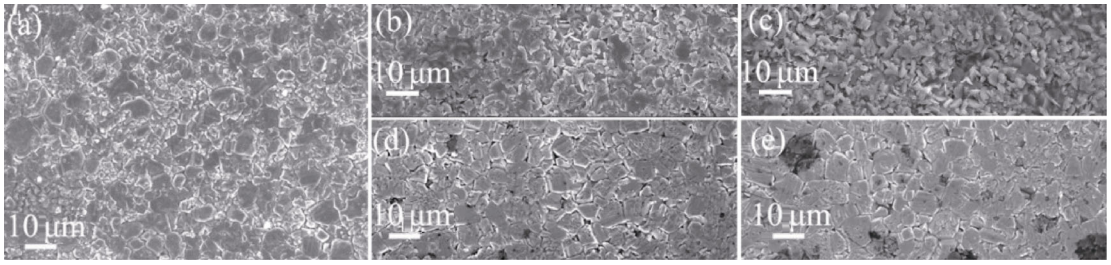

Fig. 16 Microstructural evolution of A2 ceramic during aging after (a) 0 h, (b) 200 h, and (c) 600 h, and thermal shock testing after (d) 30 and (e) 50 cycles.

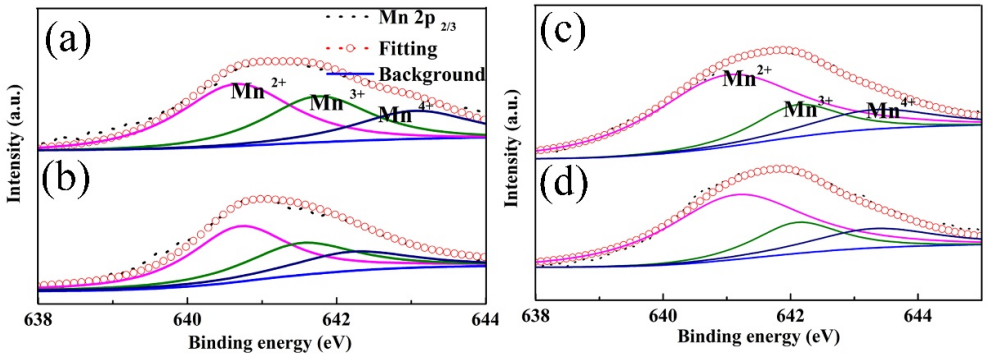

Fig. 17 High-resolution Mn $2p_{3/2}$ XPS spectra from A2 ceramic during aging after (a) 200 and (b) 600 h, and thermal shock testing after (c) 30 and (d) 50 cycles.

shock testing was reported in Ref. [17]. Moreover, the grain size of A2 ceramic increased by the thermal shock cycling.

The high-resolution Mn $2p_{3/2}$ XPS spectra from A2 samples after aging and thermal shock testing are shown in Fig. 17. As mentioned earlier, the Mn^{3+}/ Mn^{4+} ratio decreased to 1.45 and 1.42 after aging for 200 and 600 h, respectively. Similarly, the Mn^{3+}/ Mn^{4+} ratio reduced to 1.14 and 1.11 after 30 and 50 thermal shock cycles, respectively. Based on Figs. 13 and 14, the significant resistance shift between aging and thermal shock cycling can be interpreted: (1) In the case of A0 ceramic under thermal shock cycling, the precipitation of low-conductivity NiO phase resulted in a significant increase in ceramic resistance (8.9%); (2) compared with the aging performance, the thermal shock testing of A2 ceramic resulted in pore formation due to material deterioration, thus influencing the drift resistivity of ceramics; (3) the atmospheric oxygen sorption $\left(O_O^{\times} \rightarrow \frac{1}{2}O_2 + V_O^{**} + 2e'\right)$ increased with increasing pores and resulted in oxidation of Mn^{2+} to Mn^{3+}, rendering unstable configuration of cationic distribution and resistance drift, as reported in Refs. [12,52,53]; and (4) the presence of a large number of pores at grain boundaries induced a high energy barrier and reduced the time between electron scattering events of charge

carriers. Therefore, it can be concluded that the investigations based on the XRD, SEM, and XPS analysis explained the resistance shift under aging and thermal shock cycling.

4 Conclusions

In summary, Sr-doped Mn–Co–Ni ceramics have been successfully synthesized by using the co-precipitation method. The MCNS ceramics exhibited a single-phase cubic spinel structure after sintering. Furthermore, the addition of a small amount of Sr improved the density and decreased the resistivity; on the other hand, the excessive amount of Sr ($x > 0.1$) resulted in higher resistivity due to grain coarsening. Moreover, the Sr-doped MCNS ceramics demonstrated a transition from n- to p-type semiconducting behavior, which can be ascribed to Sr-doping. Impedance analysis revealed that the whole resistance of the samples was dominated by grain resistance, and conductance mechanism is that electric hole carries hopping. The aging and thermal shock rendered a similar effect on resistivity shift according to the Sr content. However, the thermal aging of MCNS ceramics exhibited a rapid resistance shift under thermal shock than the constant temperature. Besides, the thermal shock aging resulted in micro-structural evolution from highly dense to the porous structure under thermal shock testing. These results demonstrate that Sr-doping is an efficient strategy to improve the thermal stability of MCNS ceramics.

Acknowledgements

This study was supported by Xinjiang Key Laboratory of Electronic Information Materials and Devices Foundation (Grant No. 2018D04006), Tianshan Cedar Project of Xinjiang Uygur Autonomous Region (Grant No. 2018XS09), and the National Natural Science Foundation of China (Grant No. 51872326).

Electronic Supplementary Material

Supplementary material is available in the online version of this article at https://doi.org/10.1007/s40145-020-0436-z.

References

[1] Feteira A. Negative temperature coefficient resistance (NTCR) ceramic thermistors: An industrial perspective. *J Am Ceram Soc* 2009, **92**: 967–983.

[2] Han H, Park KR, Hong YR, *et al*. Effect of Fe incorporation on cation distributions and hopping conductions in Ni–Mn–Co–O spinel oxides. *J Alloys Compd* 2018, **732**: 486–490.

[3] Guan F, Lin XJ, Dai H, *et al*. $LaMn_{1-x}TixO_3$–$NiMn_2O_4$($0 \leqslant x \leqslant 0.7$): A composite NTC ceramic with controllable electrical property and high stability. *J Eur Ceram Soc* 2019, **39**: 2692–2696.

[4] Ren W, Zhu NN, Li L, *et al*. Improvement of ageing issue in $Zn_{0.4}Fe_{2.1}Co_2Mn_{1.5}O_8$ thermistor films. *J Eur Ceram Soc* 2019, **39**: 4189–4193.

[5] Liu T, Zhang HM, Ma PF, *et al*. Core–shell NTC materials with low thermal constant and high resistivity for wide-temperature thermistor ceramics. *J Am Ceram Soc* 2019, **102**: 4393–4398.

[6] Chen L, Kong WW, Yao JC, *et al*. Synthesis and characterization of Mn–Co–Ni–O ceramic nanoparticles by reverse microemulsion method. *Ceram Int* 2015, **41**: 2847–2851.

[7] Zhang M, Li MS, Zhang HM, *et al*. Synthesis of pilot-scale $Co_2Mn_{1.5}Fe_{2.1}Zn_{0.4}O_8$ fabricated by hydrothermal method for NTC thermistor. *J Alloys Compd* 2019, **797**: 1295–1298.

[8] Park K, Lee JK. The effect of ZnO content and sintering temperature on the electrical properties of Cu-containing $Mn_{1.95-x}Ni_{0.45}Co_{0.15}Cu_{0.45}Zn_xO_4$ ($0 \leqslant x \leqslant 0.3$) NTC thermistors. *J Alloys Compd* 2009, **475**: 513–517.

[9] Mhin S, Han H, Kim KM, *et al*. Synthesis of $(Ni,Mn,Co)O_4$ nanopowder with single cubic spinel phase via combustion method. *Ceram Int* 2016, **42**: 13654–13658.

[10] Yokoyama T, Meguro T, Shimada Y, *et al*. Preparation and electrical properties of sintered oxides composed of $Mn_{1.5}Co_{(0.25+x)}Ni_{(1.25-x)}O_4$ ($0 \leqslant x \leqslant 0.75$) with a cubic spinel structure. *J Mater Sci* 2007, **42**: 5860–5866.

[11] Zhang HM, Chang AM, Peng CW. Preparation and characterization of Fe^{3+}-doped $Ni_{0.9}Co_{0.8}Mn_{1.3-x}Fe_xO_4$ ($0 \leqslant x \leqslant 0.7$) negative temperature coefficient ceramic materials. *Microelectron Eng* 2011, **88**: 2934–2940.

[12] Li DF, Zhao SX, Xiong K, *et al*. Aging improvement in Cu-containing NTC ceramics prepared by co-precipitation method. *J Alloys Compd* 2014, **582**: 283–288.

[13] Mohapatra PP, Pattipaka S, Dobbidi P. The effect of Sr substitution on the electrical, dielectric and magnetic behavior of lithium ferrite. *Ceram Int* 2019, **45**: 25010–25019.

[14] Zhao S, Yue XJ, Liu X. Influence of Sr doping on structural, electrical and magnetic properties of $La_{0.7}Ca_{0.3}MnO_3$ nanoparticles. *Ceram Int* 2017, **43**: 13240–13246.

[15] Wang L, Gui MQ, Jin HB, *et al*. Temperature dependent conductivity of $Bi_4Ti_3O_{12}$ ceramics induced by Sr dopants. *J Adv Ceram* 2018, **7**: 256–265.

[16] Zhang J, Kong WW, Chang AM. Fabrication and properties of high B value $[Mn_{1.56}Co_{0.96}Ni_{0.48}O_4]_{1-x}[SrMnO_3]_x$ ($0 \leqslant x \leqslant 0.5$) spinel-perovskite composite NTC films. *J Mater Sci: Mater Electron* 2018, **29**: 9613–9620.

[17] Yang ZM, Liu H. Effects of thermal aging on the cyclic thermal shock behavior of oxide/oxide ceramic matrix composites. *Mater Sci Eng: A* 2020, **769**: 138494.

[18] Parvanian AM, Salimijazi HR, Fathi MH, *et al*. Synthesis and thermal shock evaluation of porous SiC ceramic foams for solar thermal applications. *J Am Ceram Soc* 2018, **102**: 2009–2020.

[19] Liao N, Jia DC, Yang ZH, *et al*. Enhanced thermal shock and oxidation resistance of Si_2BC_3N ceramics through MWCNTs incorporation. *J Adv Ceram* 2018, **7**: 276–288.

[20] Guillemet-Fritsch S. Structure, thermal stability and electrical properties of zinc manganites. *Solid State Ionics* 2000, **128**: 233–242.

[21] Shannon RD. Revised effective ionic radii and systematic studies of interatomic distances in halides and chalcogenides. *Acta Cryst Sect A* 1976, **32**: 751–767.

[22] Bordeneuve H, Guillemet-Fritsch S, Rousset A, *et al*. Structure and electrical properties of single-phase cobalt manganese oxide spinels $Mn_{3-x}Co_xO_4$ sintered classically and by spark plasma sintering (SPS). *J Solid State Chem* 2009, **182**: 396–401.

[23] Wang ZB, Zhao CH, Yang PH, *et al*. X-ray diffraction and infrared spectra studies of $Fe_xMn_{2.34-x}Ni_{0.66}O_4$ ($0 < x < 1$) NTC ceramics. *J Eur Ceram Soc* 2006, **26**: 2833–2837.

[24] Nolze G, Kraus W. PowderCell 2.0 for windows. *Powder Diffr* 1998 **13**: 256–259.

[25] Thakur S, Pandey OP, Singh K. A comparative structural, thermal and electrical study of Ca^{2+}, Sr^{2+} substituted $BiMnO_3$. *Solid State Ionics* 2014, **268**: 23–30.

[26] Wang JH, Yao JC, Chen ZY, *et al*. Effects of Sr-doping on the electrical properties of MnCoNiO4 NTC ceramics. *J Mater Sci: Mater Electron* 2013, **24**: 622–627.

[27] Wang XY, Li YX, Chen ZW, *et al*. Low-temperature sintering and ferromagnetic properties of $Li_{0.35}Zn_{0.30}Mn_{0.05}Ti_{0.15}Fe_{2.15}O_4$ ferrites co-fired with Bi_2O_3–MgO mixture. *J Alloys Compd* 2019, **797**: 566–572.

[28] Wang B, Wang JH, Chang AM, *et al*. Bismuth trioxide-tailored sintering temperature, microstructure and NTCR characteristics of $Mn_{1.1}Co_{1.5}Fe_{0.4}O_4$ ceramics. *RSC Adv* 2019, **9**: 25488–25495.

[29] Pugaczowa-Michalska M, Kowałczyk A, Chełkowska G, *et al*. XPS spectra and electronic structure of the $ErNi_4B$ compound. *J Alloys Compd* 2004, **385**: 44–47.

[30] Gokul B, Saravanan P, Vinod VTP, *et al*. A study on the origin of room temperature ferromagnetism in $Ni_{1-x}Gd_xO$ nanoparticles. *J Magn Magn Mater* 2015, **394**: 179–184.

[31] Anantharamaiah PN, Joy PA. Enhancing the strain sensitivity of $CoFe_2O_4$ at low magnetic fields without affecting the magnetostriction coefficient by substitution of small amounts of Mg for Fe. *Phys Chem Chem Phys* 2016, **18**: 10516–10527.

[32] Li XY, Sun Y, Zong Y, *et al*. Size-effect induced cation redistribution on the magnetic properties of well-dispersed $CoFe_2O_4$ nanocrystals. *J Alloys Compd* 2020, **841**: 155710–155717.

[33] Brabers VAM, van Setten FM, Knapen PSA. X-ray photoelectron spectroscopy study of the cation valencies in nickel manganite. *J Solid State Chem* 1983, **49**: 93–98.

[34] Wei WF, Chen WX, Ivey DG. Rock salt–spinel structural transformation in anodically electrodeposited Mn–Co–O nanocrystals. *Chem Mater* 2008, **20**: 1941–1947.

[35] Ngida REA, Zawrah MF, Khattab RM, *et al*. Hydrothermal synthesis, sintering and characterization of nano La-manganite perovskite doped with Ca or Sr. *Ceram Int* 2019, **45**: 4894–4901.

[36] Polfus JM, Yildiz B, Tuller HL. Origin of fast oxide ion diffusion along grain boundaries in Sr-doped $LaMnO_3$. *Phys Chem Chem Phys* 2018, **20**: 19142–19150.

[37] Zhang B, Zhao Q, Chang AM, *et al*. La_2O_3-doped $0.6Y_2O_3$–$0.4YCr_{0.5}Mn_{0.5}O_3$ composite NTC ceramics for wide range of temperature sensing. *J Alloys Compd* 2013, **581**: 573–578.

[38] Park K, Han IH. Effect of Al_2O_3 addition on the microstructure and electrical properties of $(Mn_{0.37}Ni_{0.3}Co_{0.33-x}Al_x)O_4$ ($0 \leqslant x \leqslant 0.03$) NTC thermistors. *Mater Sci Eng: B* 2005, **119**: 55–60.

[39] Jadhav RN, Puri V. Influence of copper substitution on structural, electrical and dielectric properties of $Ni_{(1-x)}Cu_xMn_2O_4$ ($0 \leqslant x \leqslant 1$) ceramics. *J Alloys Compd* 2010, **507**: 151–156.

[40] Yokoyama T, Abe Y, Meguro T, *et al*. Preparation and electrical properties of sintered bodies composed of monophase spinel $Mn_{(2-x)}Co_{2x}Ni_{(1-x)}O_4$ ($0 \leqslant x \leqslant 1$) derived from rock-salt-type oxides. *Jpn J Appl Phys* 1996, **35**: 5775–5780.

[41] Dannenberg R, Baliga S, Gambino RJ, *et al*. Resistivity, thermopower and the correlation to infrared active vibrations of $Mn_{1.56}Co_{0.96}Ni_{0.48}O_4$ spinel films sputtered in an oxygen partial pressure series. *J Appl Phys* 1999, **86**: 514–523.

[42] Li M, Pietrowski MJ, de Souza RA, *et al*. A family of oxide ion conductors based on the ferroelectric perovskite $Na_{0.5}Bi_{0.5}TiO_3$. *Nat Mater* 2014, **13**: 31–35.

[43] Gao ZP, Wu LF, Lu CJ, *et al*. The anisotropic conductivity of ferroelectric $La_2Ti_2O_7$ ceramics. *J Eur Ceram Soc* 2017, **37**: 137–143.

[44] Nobre MAL, Lanfredi S. Thermistor ceramic with negative temperature coefficient based on $Zn_7Sb_2O_{12}$: An inverse spinel-type phase. *Appl Phys Lett* 2002, **81**: 451–453.

[45] Li RF, Fu QY, Zou XH, *et al*. Mn–Co–Ni–O thin films prepared by sputtering with alloy target. *J Adv Ceram* 2020, **9**: 64–71.

[46] Behera B, Nayak P, Choudhary RNP. Impedance spectroscopy study of $NaBa_2V_5O_{15}$ ceramic. *J Alloys Compd* 2007, **436**: 226–232.

[47] Sun X, Leng SL, Zhang H, *et al*. Electrical properties and temperature sensitivity of Li/Mg modified $Ni_{0.7}Zn_{0.3}O$ based ceramics. *J Alloys Compd* 2018, **763**: 975–982.

[48] Guiffard B, Boucher E, Eyraud L, *et al*. Influence of donor co-doping by niobium or fluorine on the conductivity of

Mn doped and Mg doped PZT ceramics. *J Eur Ceram Soc* 2005, **25**: 2487–2490.

[49] Feltz A. Perovskite forming ceramics of the system ($Sr_xLa_{1-x}Ti_{x+y}Co_yCo_{1-x-2y}O_3$) for NTC thermistor applications. *J Eur Ceram Soc* 2000, **20**: 2367–2376.

[50] Peng CW, Zhang HM, Chang AM, *et al*. Effect of Mg substitution on microstructure and electrical properties of $Mn_{1.25}Ni_{0.75}Co_{1.0-x}Mg_xO_4$ ($0 \leqslant x \leqslant 1$) NTC ceramics. *J Mater Sci: Mater Electron* 2012, **23**: 851–857.

[51] Groen WA, Zaspalis V, Schuurman S. Aging of NTC ceramics investigated by magnetic measurements. *J Mater Sci Lett* 1999, **18**: 1233–1235.

[52] Zhao CH, Wang BY, Yang PH, *et al*. Effects of Cu and Zn co-doping on the electrical properties of $Ni_{0.5}Mn_{2.5}O_4$ NTC ceramics. *J Eur Ceram Soc* 2008, **28**: 35–40.

[53] Fritsch S. Correlation between the structure, the microstructure and the electrical properties of nickel manganite negative temperature coefficient (NTC) thermistors. *Solid State Ionics* 1998, **109**: 229–237.